Article:
Deng, F. and Qin, N. (2021) Vortex-generating shock control bumps for robust drag reduction at transonic speeds. AIAA Journal, 59 (10). pp. 3900-3909. ISSN: 0001-1452

https://doi.org/10.2514/1.j060528

Vortex Generating Shock Control Bumps for Robust Drag Reduction at Transonic Speeds

F. Deng[1] and N. Qin[2]

Abstract: The 3D contour bump has been integrated with vane-type vortex generators (abbreviated as VGs) to weaken the shock wave and suppress potential flow separation at higher transonic speeds. The integrated vortex generating shock control bump is parameterized as a whole, in a manner that the contour bump is designed for shock control and the vortex generating fins are integrated to the contour bump for separation control. This allows the balance between the two factors affecting the total wing drag. The optimization studies based on the Reynolds-average Navier-Stokes equations have been carried out to find the optimal vortex generating bump designs at the given design conditions. Single-point and multi-point global optimizations are carried out to search the optimum parameters at the corresponding design points. It is found that the vortex generating bump can further reduce the total drag at the higher transonic Mach numbers due to the alleviation of after-bump streamwise separation by a pair of counter-rotating vortices generated. The inclusion of the VGs in the bump design allows for a better balance of the design in controlling both the shock strength and the flow separation after the bump at higher Mach numbers. A multi-point optimization leads to a robust vortex generating bump design for a range of Mach numbers. The distinctive vortical flow structures induced by the vortex generating bump are highlighted and discussed.

Keywords: Shock Control Bump, Vortex Generator, Drag Reduction, Flow Separation, Aerodynamic Shape Optimization.

[1] Lecturer, College of Aerospace Engineering, Nanjing University of Aeronautics and Astronautics, Nanjing, China; Visiting Researcher, Department of Mechanical Engineering, The University of Sheffield, Sheffield, S1 3JD, UK

[2] Professor, Department of Mechanical Engineering, The University of Sheffield, Sheffield, S1 3JD, UK, Corresponding author: n.qin@sheffield.ac.uk, Associate Fellow AIAA.

1 Introduction

For aircraft flying at transonic speeds, the wave drag due to the appearance of shock waves and the parasite drag by shock-induced separations are two main components of the overall drag. Numerous methods have been developed for reducing shock wave drag [1]. In order to explore the potential of applying natural laminar flow technology at a higher Mach number for future aircraft, two European projects, EUROSHOCK I [2] and EUROSHOCK II [3] had concluded that local contour bumps are the most efficient shock control devices in terms of drag reduction. This motivated further research on shock control bumps for transonic flight.

The concept of shock control bump can be traced back to Tai's work in the late 1970s [4] and its effectiveness on drag reduction had been confirmed by an experimental investigation [5]. Later, Ashill and Fulker [6, 7] applied local 2D bumps to reduce shock wave drag on laminar flow airfoils. Since then, several types of shock control bump, including contour and wedge-shaped bumps, have been extensively investigated by both computational and experimental studies [2, 3, 8-15]. The dominant drag reduction mechanism is either the weakening of the shock wave or the turning of the shock into continuous compression waves, resulting in the reduction of the wave drag. Due to the delay of shock induced separation through shock control, the drag rise Mach number is increased as a result. Bruce and Colliss [16] gave a comprehensive review on the early work on shock control bump research.

More recent studies on shock control bumps have turned into more practical problems. In 2013, Deng *et al*. [17] put an array of optimized 3D contour bumps on a low-sweep supercritical wing and achieved the same cruise drag as that with a higher sweep angle. Later, Jones *et al.* [18] investigated numerically the applications of 3D wedge-shaped bumps on an infinitely swept wing and concluded that well-designed 3D bumps on swept wings could offer drag reductions comparable to those on unswept wings. At the same time, the wind tunnel tests conducted by Zhou *et al.* [19] confirmed that the 3D contour bumps on a supercritical swept wing offered better drag reductions in comparison

with other passive shock control methods. The work by Hinchliffe and Qin [20] provides a new efficient way to optimize shock control bumps on wings. Then, Jones *et al.* [21] extended their numerical works to a transonic wing-body model and confirmed the results as their previous study. More recently, Zhu *et al.* [22] conducted a combined experimental and computational study of a low-sweep transonic natural laminar flow wing with contour shock control bumps. The experiment was specifically designed with solid wind-tunnel wall conditions for comparison with numerical results. The study shows that the strong shock wave on the low-sweep natural laminar flow wing can be effectively controlled by optimized bumps. Deng and Qin [23] compared 2D and 3D bumps in the context of local transonic area rule in a recent work. It was found that one of the crucial parameters of 2D and 3D bumps is their cross-sectional area that can be explained by applying the classical transonic area rule.

One difficulty associated with applications of shock control bumps is their sensitivity to the shock wave position, resulting in poor off-design performances. In order to address this issue, adaptive shock control bumps were advocated by Birkemeyer *et al.* [8]. The adaptive shock control bumps were further developed by Jinks *et al.* [24] with the consideration of structural design requirements. Gramola *et al.* [25, 26] conducted a series of experiments, trying to understand the physics of 2D adaptive shock control bumps from the perspective of flow and structural interaction. The off-design performances were also studied with the suggestions that some constraints are needed to achieve desirable surface deformations.

For adaptive shock control bumps, there is a penalty of structure complexity increasing aircraft's weight and maintenance costs. Some researchers tried to exploit the characteristics of shock control bumps at off-design conditions through more robust designs. Wong *et al.* [12] and Ogawa *et al.* [13] observed the existence of streamwise vortices after 3D ramp bumps. Later, the vortical structures were further investigated by Colliss *et al.* [15] in a joint experimental and computational study. Considering the potential applications, Eastwood and Jarrett [27] conducted a study on 3D bumps and discovered that the streamwise vortices produced could increase the buffet margin due to their

capability of suppressing separated flow at high transonic Mach numbers. Tian *et al.* [28] investigated 2D contour shock control bumps in terms of transonic buffet control and found that they could improve the buffet performance. More recently, Mayer *et al.* [29] assessed both 2D and 3D bumps for buffet control. They also tuned the vortical wake of 3D bumps by shaping of the bumps' side flanks but with an unfavorable deterioration of the bump's ability to reduce shock strength. Later, Mayer *et al.* [30] extended their study to a wing-body configuration and investigated three types of shock control bumps. They found that all three bumps achieved desirable behaviors while 3D wedge-shaped bumps did not perform as well as expected. It is likely due to a mismatched cross-sectional area with that of 2D bumps as shown in our earlier study [23].

From the review above, one of the attractions of 3D wedge-shaped bumps is their ability of producing streamwise vortices that could be useful in suppressing flow separations downstream of the bumps. The vortical flows appear as the by-products of their sharp edges. The vortices are usually weak [15, 27, 29] and hard to control without affecting the effectiveness of shock control as shown in the study by Mayer *et al.* [29]. As this type of 3D bumps is designed for shock control, their capability in suppressing flow separation is unknown. The present study takes a different strategy through explicitly integrating contour bumps for shock control and vortex generators for downstream separation control for more robust performance at transonic speeds.

The vortex generators (abbreviated as VGs), including vane-type or wheeler-type, are well studied in reducing flow separations at different speeds [31-33]. For design optimization of the vortex generating bump, the vortex generators are allowed to move freely on the bump surfaces and explicitly optimized for specified purposes. This work will focus on assessing their abilities for robust design through the combined effects on both shock control and alleviation of the after-bump separation.

The paper first propose a new parameterization method for coupling the 3D contour bump and vane-type vortex generators as an integrated device. For the optimal design, an efficient global

optimization method is used to find the optimum designs for the given conditions. Single point optimization is presented first for different Mach numbers. This is followed by a multi-point optimization for robust design for a range of Mach numbers. The vortical structures induced by the vortex generating fins and associated flow physics are analyzed, before the paper is concluded.

2 Parameterization of vortex generating bump

The parameterization method for 3D contour shock control bumps proposed by Qin *et al.* [10] is used, as shown in Fig. 1. The geometry of a bump is determined by six key design variables, including bump length (*L*), bump height (*H*), bump crest (x_{crest}), relative crest (*R*), relative bump span (*RS*) and total sectional span (*TS*). Note that the total sectional span refers to the width of the 3D simulation. The bumps are added on the top of a given baseline wing surface and the bump function represents the distance between the baseline wing and the bump surface. The streamwise bump profile is represented by two third order polynomials, denoted as $y_1(x,z)$ and $y_2(x,z)$. Their equations can be written as

$$y_1(x_{start},z) = y_2(x_{end},z) = 0 \tag{1a}$$

$$y_1'(x_{start},z) = y_2'(x_{end},z) = 0 \tag{1b}$$

$$y_1(x_{crest},z) = y_2(x_{crest},z) = y_3(z) \tag{1c}$$

$$y_1'(x_{crest},z) = y_2'(x_{crest},z) = 0 \tag{1d}$$

where $x_{start} = x_{crest} - L \times R$ is the starting point of the bump and $x_{end} = x_{start} + L$ is the endpoint of the bump. The gradients at the starting point and the endpoint are both set to zero to enforce a tangential condition (C^1) at the intersection points between the bump geometry and the baseline wing. The spanwise profile is also represented by a third order polynomial, denoted as $y_3(z)$, satisfying the following conditions:

$$y_3(z_{crest}) = H \tag{2a}$$

$$y_3'(z_{crest}) = 0 \tag{2b}$$

$$y_3(z_{end}) = 0 \tag{2c}$$

$$y_3'(z_{end}) = 0 \tag{2d}$$

where z_{crest} is the spanwise position of the maximum crest of the bump and $z_{end} = z_{crest} + TS \times RS$.

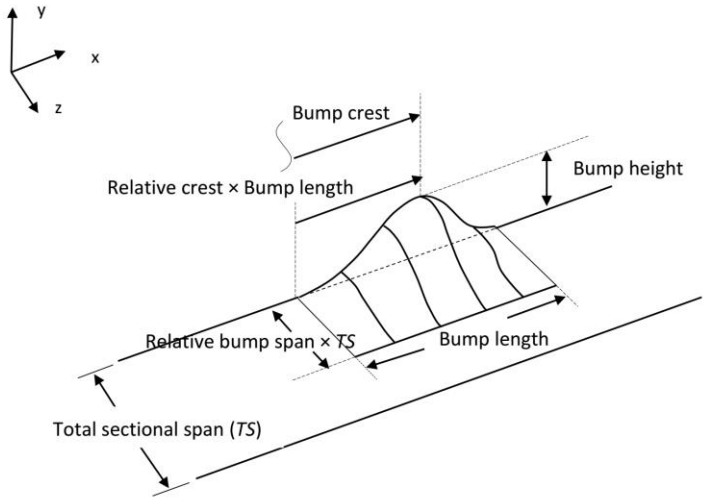

Fig. 1 Parameterization of 3D contour shock control bumps [10].

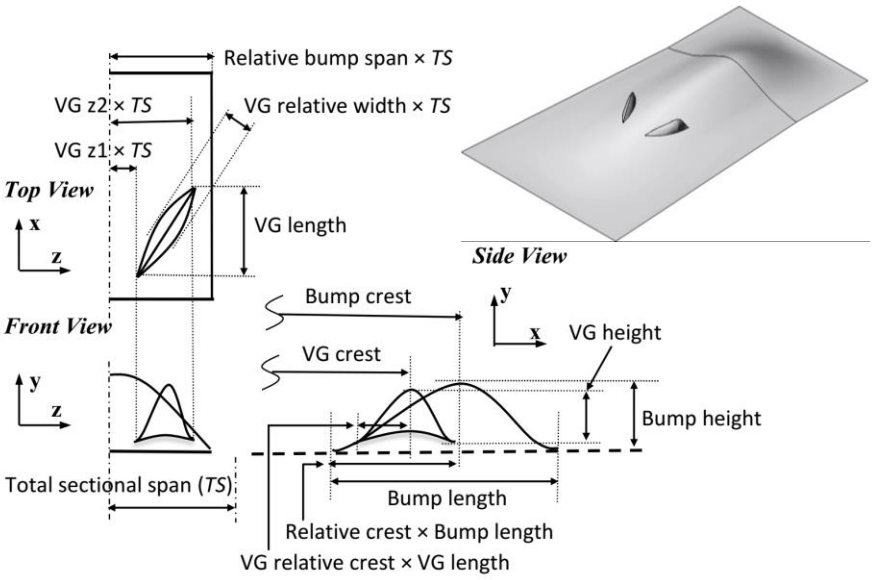

Fig. 2 Parameterization of vortex generating bumps.

In order to allow contour shock control bumps to produce streamwise vortices effectively, two vane-type vortex generating fins are attached to the bump surface. The integrated design is shown in Fig.2. The two vortex generating fins are assumed to be put on the top of a baseline bump and symmetrical with respect to z-axis. The vortex generating fins are defined by seven additional design variables, named with "VG" in the figure. They are the VG length, VG height, VG crest, VG relative crest and VG relative width. The VG z1 and VG z2 are two design variables used to specify the spanwise locations of vortex generating fins. One key design parameter, the angle between the vortex generating fins and local flow velocity, is also implicitly specified by VG z1 and VG z2. The profile of a vortex generating fin along its centre line is the same as Eq. (1), except that $y_3(z)$ is replaced by a quadratic polynomial, which can be defined by Eq. (2a, 2c, 2d). The Eq. (2b) is removed with the purpose of ensuring sharp edges for effective vortex generation. In total, thirteen design variables are needed to define a vortex generating bump.

3 Optimization study

3.1 Problem definition

In order to explore the design space of the proposed vortex generating bump parameterized in Fig. 2, the following multi-point drag minimization problem is posed:

$$\begin{aligned} &\min\left(\sum_{n=1}^{m} \omega_n \times C_{D,n}(\boldsymbol{DV})\right) \\ &s.t.\ \boldsymbol{b_l} < \boldsymbol{DV} < \boldsymbol{b_u} \end{aligned} \tag{3}$$

where $\boldsymbol{DV}$ is the continuous vector for the free design variables of the bumps, and $\boldsymbol{b_l}$ and $\boldsymbol{b_u}$ are their lower and upper bounds, respectively. $C_{D,n}$ represents the drag coefficient at the n-th design point with a weighting coefficient ω_n specified by users, satisfying $\sum_{n=1}^{m} \omega_n = 1$. During the following optimizations, the lift coefficient C_L will be kept constant by the CFD solver by allowing the angle of attack to be adjusted.

3.2 Numerical methods

The optimization of shock control bump involves highly nonlinear flow phenomena, such as shock-boundary-layer interaction and flow separation. Using gradient-based optimization, it was found that local searches starting with different initial design points may lead to different optima, indicating that the design spaces contained multiple local optima. In order to find the global optimum, the Efficient Global Optimization (EGO) method [34, 35] that automatically balances the local exploitation and global exploration is employed in the present optimization. The optimization algorithm assisted by the Kriging surrogate model has been proved to be suited for high-fidelity aerodynamic shape optimization [23]. To enhance its local search ability, after the EGO search, a derivative-free optimizer, named BOBQYA, by Powell [36] is used to further improve the results. The combination of EGO and BOBQYA optimizers provides a highly efficient way to search the global optimum in the design space spanned by vortex generating bump design variables.

For the Reynolds-average Navier-Stokes solution, the open source code CFL3D v6.7 developed at NASA [37] is adopted in this work. It is a multiblock structured CFD solver equipped with a cell-centered finite volume scheme and a number of turbulence models. The code has been tested for a large number of test cases, including a recent validation of the Common Research Model created for the Fifth Drag Prediction Workshop [38]. For this work, a test case of RAE5243 airfoil with the data measured in the wind tunnel experiment by Fulker and Simmons [39] has been adopted to validate the CFD solver and numerical settings. The RAE5243 airfoil has a maximum thickness of $14\%c$ and a trailing edge angle of 10^{o}. It will be used as the baseline for the present work. The mesh around the RAE5243 airfoil is a multi-block structured C-type mesh with 249×129 grid points as shown in Fig.3(a). The lift-coefficient C_L is specified as that in the experiment. The Roe approximate Riemann solver with the third-order MUSCL interpolation is employed for the discretization of convective terms and the second-order center scheme is used for the viscous terms. Two turbulence models that are widely used in external aerodynamic flows, namely Menter's SST two equation turbulence model (SST) [40] and the Spalart Allmaras one equation turbulence model (SA) [41], are chosen in the

validation case. The computational results are compared with the experimental data in Table 1 and Fig. 3(b). In terms of drag prediction, Menter's SST model produces a better comparison with the experimental data. The relative errors of using the SA model and SST model are 12.2% and 4.1%, respectively. Allan *et al.* [42] also found that Menter's SST model provide much better predictions for separated flows for a low-profile vortex generating vane. In the study of vortical flows around 3D bumps by Colliss *et al.* [15], Menter's SST model was also chosen and a good agreement with the experiment data was achieved. Based on this analysis, Menter's SST model has been chosen in this study. The flow around the wing section is assumed to be fully turbulent in the following studies.

Table 1 Comparison of drag coefficients at M_∞=0.6799, Re_c=18.68×10^6 and C_L=0.5154.

Experiment [39]	SA	SST
0.00877	0.00984	0.00913

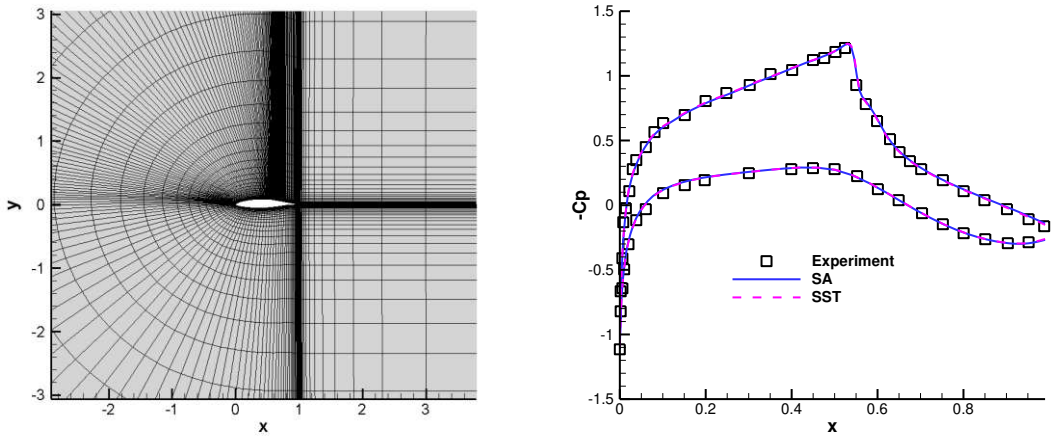

(a) Mesh (b) Pressure coefficient

Fig. 3 Validation case at M_∞=0.6799, Re_c=18.68×10^6 and C_L=0.5154.

3.3 Results and discussions

3.3.1 Optimization setup

An infinite unswept (2D) wing with RAE5243 airfoil section is selected as the baseline to accommodate 3D vortex generating shock control bumps. A half of bump will be simulated by

applying a symmetry boundary condition in the centerline of the bump and a periodic boundary condition at the other end in the spanwise direction. Note that the results of a whole bump will be presented for better understanding. A structured C-type mesh similar to the one shown in Fig. 3(a) is adopted for the wing section. To maintain the quality of mesh around the sharp edges of vortex generating fins, the surface mesh have been split into two domains as shown in Fig. 4. After each update of surface geometry and mesh, an algebraic grid deformation technique [17] is employed to deform the volume mesh. It propagates the changes of surface mesh points into outside space along the mesh lines normal to the wall. In order to choose a proper mesh size, a mesh sensitivity study was carried out with one of the optimized vortex generating bumps as shown in Fig. 4. The results are presented in the Table 2. Based on this analysis, the mesh with 249×129×65 grid points is chosen in the optimizations that required roughly O(10^2) numbers of CFD simulations.

Table 2 Mesh sensitivity study at M_∞=0.7, Re_c=18.68×10^6 and C_L=0.82.

Number of grid points	C_D
125×65×33	0.01863
249×65×33	0.01905
249×129×33	0.01921
249×129×65	0.01930
497×257×129	0.01941

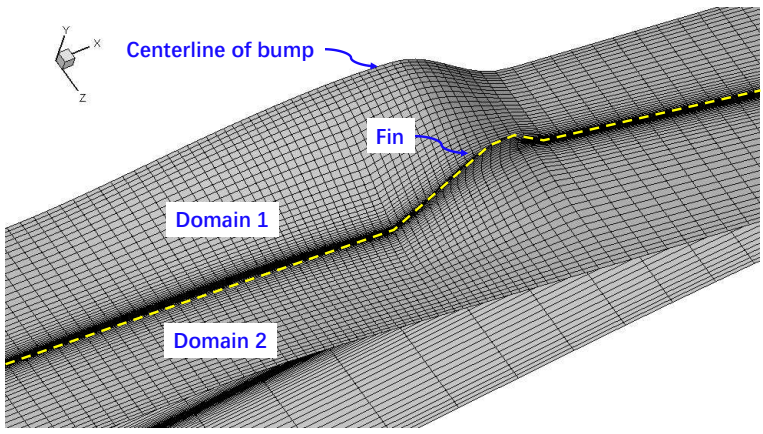

Fig. 4 Surface mesh for vortex generating bumps.

Following our previous work [23], the three most sensitive design variables, including bump crest, relative crest and bump height, are chosen for contour bump optimizations. The bump length, relative bump span and total sectional span are fixed as 0.3c, 80% and 0.119c, respectively. Four additional key VG design variables, including VG height, VG crest, VG z1 and VG z2 are used for optimizing vortex generating bumps while VG length, VG relative crest and VG relative width are fixed as 0.1c, 80% and 10%, respectively.

3.3.2 Single-point optimizations

In order to investigate the behavior of the optimized vortex generating bumps as freestream Mach number rises, following our previous work [23], a number of optimizations have been performed at a range of freestream Mach numbers, i.e. M_∞=0.68, 0.69, 0.70, 0.71 and 0.72, with C_L=0.82 and Re_c=18.68×10^6. The location of shock wave on the upper surface varies in the range of 40%～55% chord correspondingly.

The optimization results are given in Tables 3&4 and Fig. 5. Table 3 shows the results for bump only optimization at different Mach numbers. Clearly as the Mach increases, the effectiveness of shock control increases accordingly using the optimized bumps. Table 4 shows the optimization results for the vortex generating bump at different Mach. It is noted that at the lower Mach numbers of 0.68 and 0.69, the optimization does not trigger the VGs to feature in the device. This can be explained by the fact that at these conditions, no streamwise separation is induced downstream of the bump. However, at M_∞ equal or greater than 0.7, two counter-rotating vortex generating fins emerge through optimization, with further drag reduction compared to corresponding contour bumps. The improvement of drag reduction reaches to 49.7% at M_∞=0.72, with an additional 19.8% from the integration of vortex generating fins. The optimized VG height is the same order as undisturbed local boundary layer thickness. Also noted in Fig. 5(b) is that the integration of the vortex generating fins enables the bump height to increase 5%～11% compared to corresponding contour bump. Based on these observations, at the higher Mach numbers, vortex generating fins can alleviate the bump

induced streamwise separation and enable a more robust performance of the vortex generating bump for shock control. Fig. 6 shows that the optimized vortex generating fins move upstream as freestream Mach number increases, indicating that the location of optimized vortex generating fins is sensitive to the freestream Mach number.

Table 3 Optimization results of contour bumps.

M_∞	C_D (Improvement)	C_D of baseline	Bump crest	Relative crest	Bump height
0.68	0.01237 (19.1%)	0.01529	0.6183c	54.0%	0.0136c
0.69	0.01593 (24.0%)	0.02098	0.6396c	55.2%	0.0220c
0.70	0.02121 (28.3%)	0.02959	0.6767c	70.1%	0.0334c
0.71	0.02878 (32.5%)	0.04264	0.6836c	77.7%	0.0387c
0.72	0.04177(29.9%)	0.05959	0.6237c	69.1%	0.0379c

Table 4 Optimization results of vortex generating bumps.

M_∞	C_D (Improvement)	Bump crest	Relative crest	Bump height	VG crest	VG height	VG z1	VG z2
0.68	0.01237 (19.1%)	0.6183c	54.1%	0.0136c	0.0	0.0	0.0	0.0
0.69	0.01593 (24.0%)	0.6396c	55.3%	0.0220c	0.0	0.0	0.0	0.0
0.70	0.01930 (34.7%)	0.6988c	73.2%	0.0358c	0.7382c	0.0129c	58.9%	35.9%
0.71	0.02358(44.7%)	0.7158c	71.4%	0.0409c	0.6556c	0.0073c	59.6%	39.9%
0.72	0.02996 (49.7%)	0.7165c	70.5%	0.0421c	0.5421c	0.0078c	59.0%	38.3%

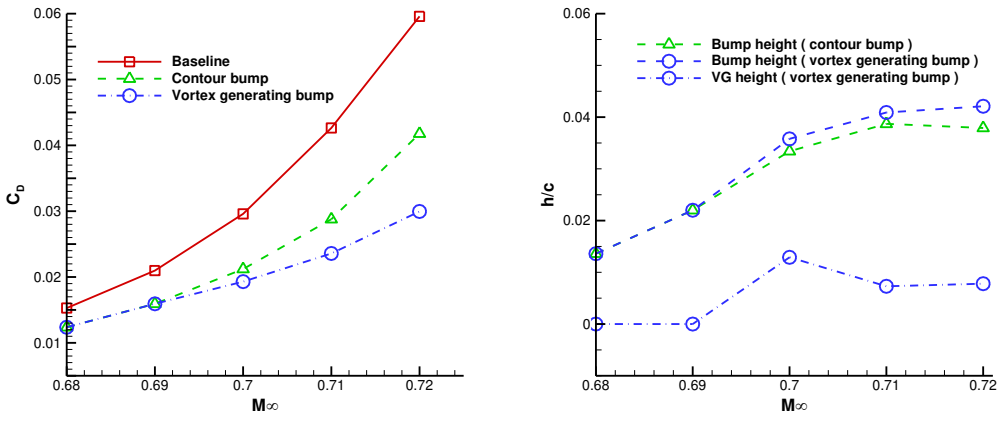

(a) Drag coefficient (b) Height

Fig. 5 Single-point optimizations at each Mach number with C_L=0.82.

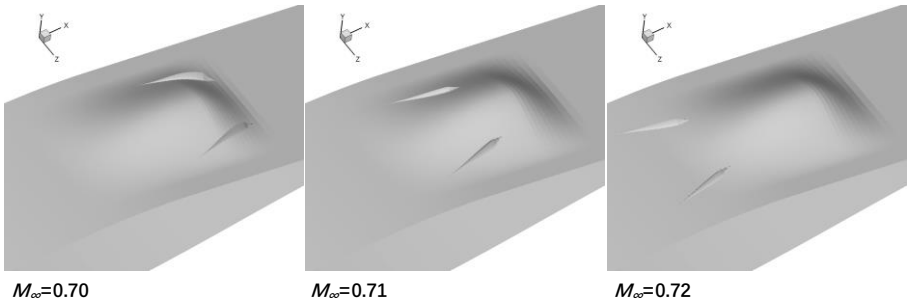

Fig. 6 Comparison of geometries of optimized vortex generating bump.

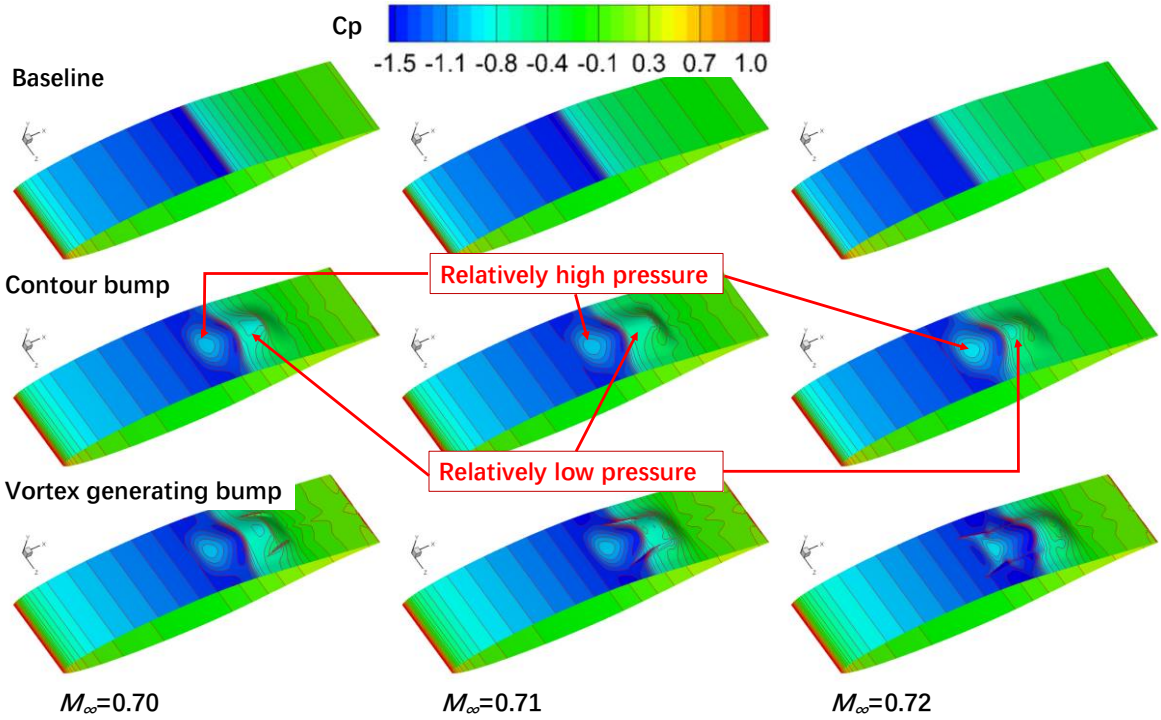

Fig. 7 Comparison of contours of surface pressure coefficient.

The pressure footprints on the upper surface are shown in Fig. 7. They show that the controlled shock waves are curved in the spanwise direction due to variations of local bump heights. It is apparent that the streamwise position of vortex generation fins depends on the shock strength. At M_∞=0.70, the optimized vortex generating fins have minor effects on the upstream shock wave control since they are located after the shock wave. Above M_∞=0.70, the controlled shock waves are disturbed by the

vortex generating fins located near or before the shock waves. This can be attributed to the requirement of stronger vortices for the high Mach cases.

To look into the streamwise flow separation, Fig. 8 shows the comparison of skin friction lines and the extent of flow separation. The extent of flow separation is judged by the reversed flow at wall (negative streamwise component of skin friction), which is indicated by dark color in the figure. As M_∞ increases, shock-induced separation becomes severer until the flow separation region accounts for almost 60% of the baseline wing surface at M_∞=0.72. With optimized shock control bumps, shock-induced separations are suppressed partially, due to the weakening of shock waves. However, further separation bubbles after the bump crest occur due to an increase of bump height. This indicates that there is a trade-off between shock control and flow separation after the bump crest. At higher Mach numbers, an increase of the bump height is demanded by wave drag reduction but at the cost of flow separations. This problem is relieved by vortex generation bumps. At M_∞ equal or greater than 0.7, in contrast to shock control bumps causing severe flow separations, the optimized vortex generating bumps can alleviate flow separations. The extent of flow separations are limited to the relatively small areas near two vortex generating fins.

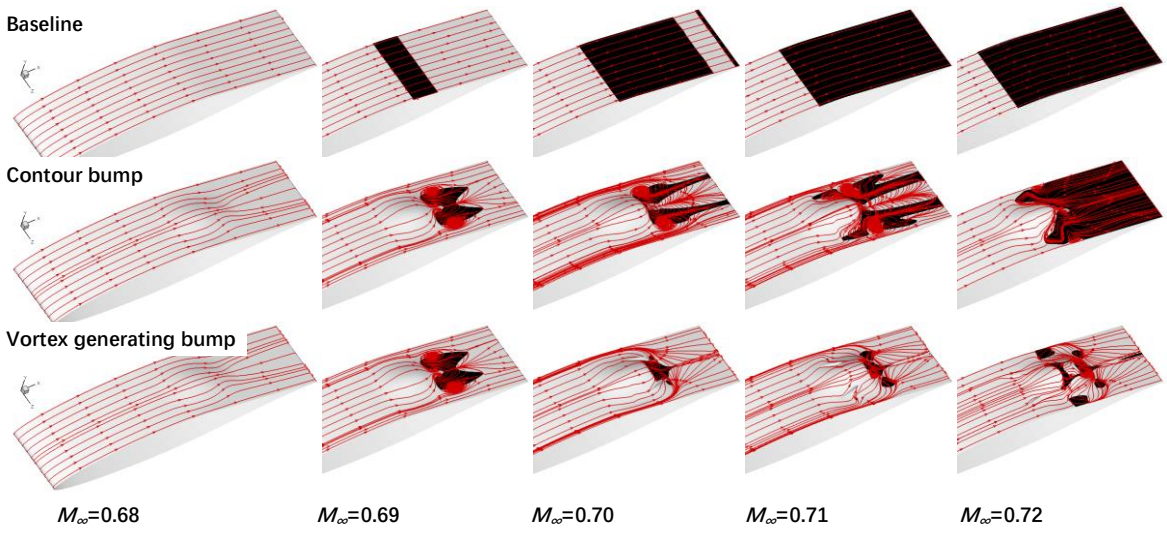

Fig. 8 Comparison of skin friction lines and flow separation area (dark color).

The existence of streamwise vortices in the flowfield of a 3D wedge bump was observed by Wong *et al.* [12] and Ogawa *et al.* [13]. Later, there were researches on understanding the flow physics and potential in applications [15, 27, 29]. Although the flow mechanism of their production is still debated, it is anticipated that 3D wedge bumps could work as "smart" vortex generators to improve their off-design performances. However, it was discovered that the intensity of those streamwise vortices was rather weak, without playing a significant role in separation control [29]. As shown here, the integrated vortex generating bumps are able to produce strong streamwise vortices to suppress flow separations at high transonic Mach numbers.

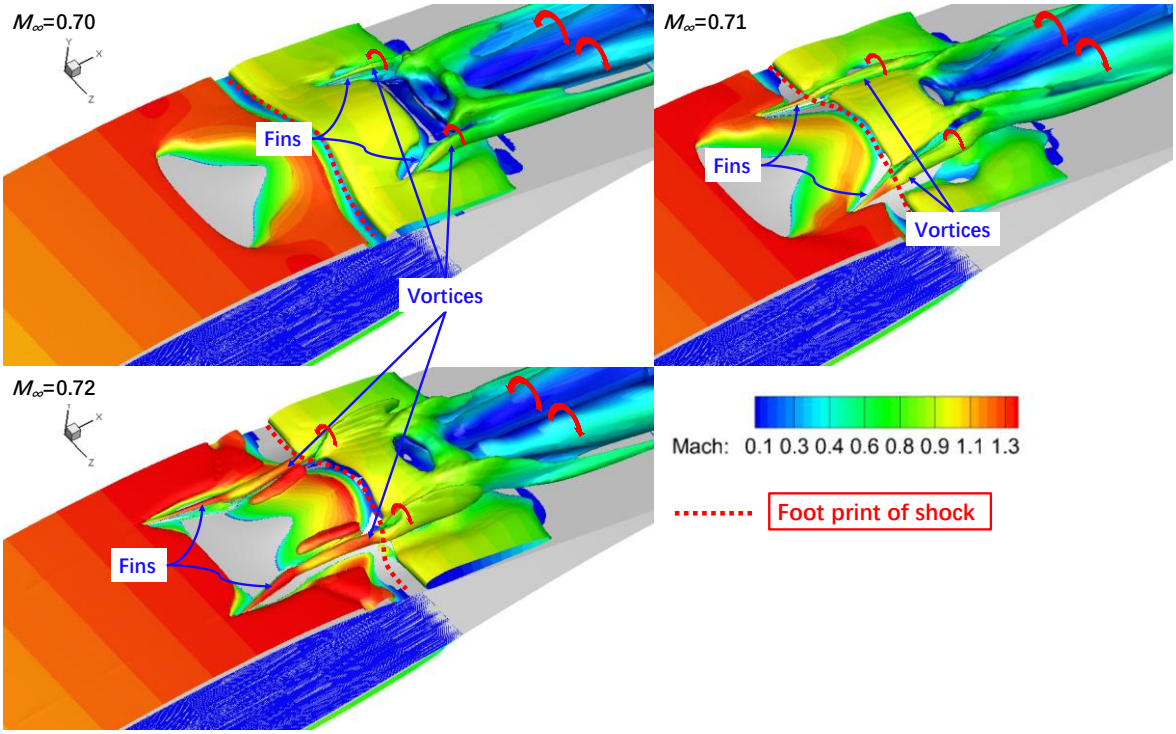

Fig. 9 Iso-surfaces of vortex generating bumps (*Q* criterion = 1).

The vortical structures in the flowfields of vortex generating bumps are visualized by the *Q* criterion in Fig. 9, which shows the iso-surfaces of *Q* criterion = 1. The local Mach number is shown by the colors on the iso-surfaces. A pair of streamwise vortices after the vortex generating bump are clearly seen downstream of the bump. Two small vortices can also be clearly seen after the vortex generating fins. After leaving the fins, these two vortices continue to expand their sizes while moving

downstream along the streamwise direction. Note for M_∞=0.71 and 0.72, the fin induced vortices start before the footprint of the shock. The more forward optimized fins for the higher Mach cases may be attributed to the demand for stronger vortices to alleviate the larger streamwise separation, referring back to Fig. 8.

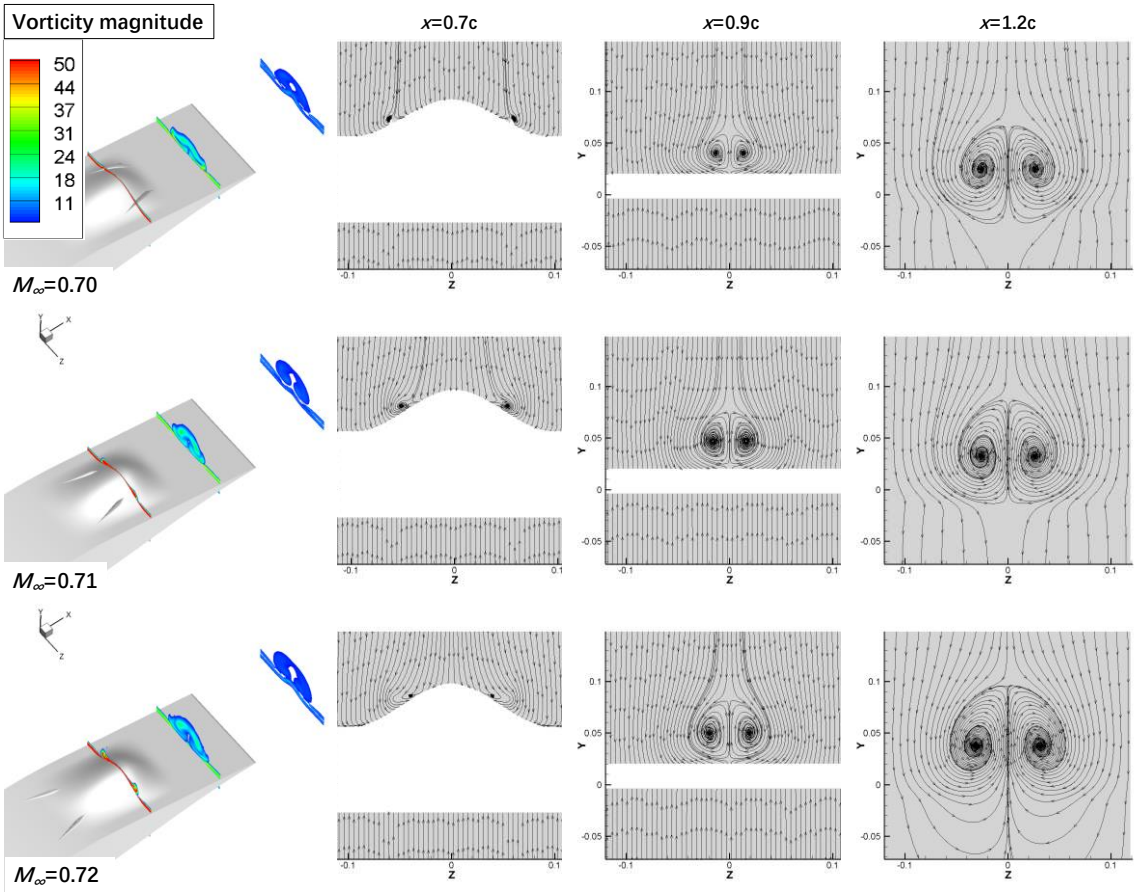

Fig. 10 Comparison of cross-sectional slices of vortex generating bumps.

Further details of vortical structures are shown by three cross-sectional slices in Fig. 10. The contours of vorticity magnitude and cross-sectional streamlines are examined at the positon of x=0.7c, 0.9c and 1.2c. A pair of counter-rotating vortices are clearly shown. The right vortex rotates in a clockwise direction, seen from the bump leading edge. From x=0.7c to x=0.9c, the vortex size increase significantly. This confirms the observations made previously. The contours of vorticity magnitude also indicate the relation of the thin boundary layers and the vortex wakes.

The topologies of surface skin friction lines around vortex generating bumps are compared in Fig.11. Although there are still some small shock-induced flow separation at M_∞=0.72, the same flow topology, that consists of two saddles and two focuses, is independent on freestream Mach number and the locations of upstream vortex generating fins. The second saddle denoted as "S2" in the figure is followed by two separation lines caused by two streamwise vortices.

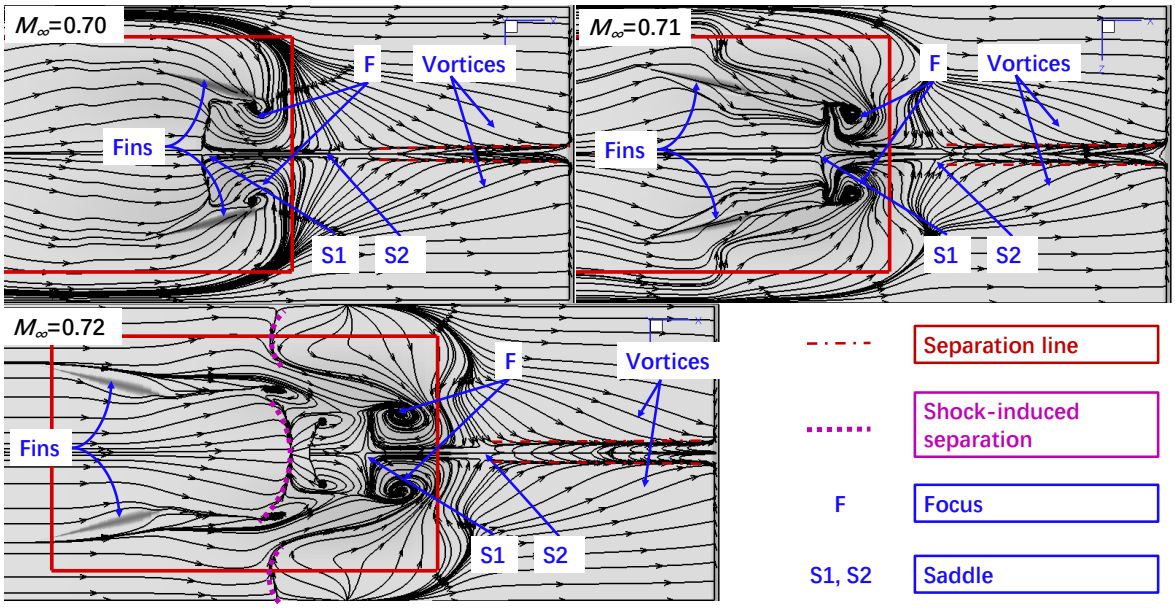

Fig. 11 Comparison of skin friction lines of vortex generating bumps.

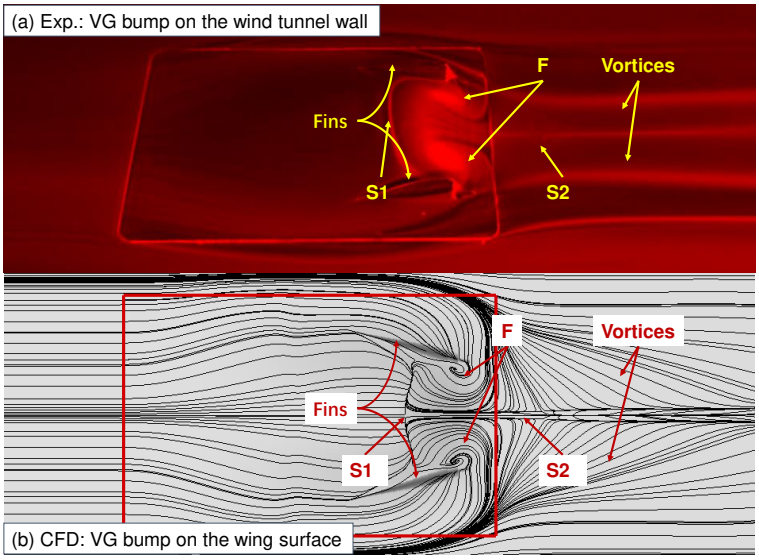

Fig. 12 Comparison of flow topologies from the experiment (oil flow) and simulation (skin friction lines).

The authors have provided the vortex generating bump model optimized at M_∞=0.70 to Lo and Kontis[43] for experimental investigation. In the wind tunnel test, the model was installed on the wind tunnel wall in a supersonic stream at a freestream Mach of 1.3, which is close to the local maximum Mach number on the wing surface as shown in Fig. 9. The bump geometries in the simulation and experiment are the same while the flow conditions are similar in relation to the Mach number at the bump position. In Fig. 12, the surface flow topology between the experiment and the simulation is compared qualitatively. Notably, the pattern of skin friction lines after the bump crest is similar to the surface oil flow pattern in the experiment.

3.3.3 Multi-point optimizations

In principle, the vortex generating bumps could be designed as active control devices with optimum performances at each operating Mach number. Although the trade-off between structure complexity and aerodynamic performance needs to be elaborately considered in practice, this problem may be solved in the future with the advancement of "smart" structures as discussed the recent works by Jinks *el al.* [24] and Gramola *et al.* [25, 26]. In practices, passive controls are more favorable because of their simplicity and low maintenance costs. To find a vortex generating bump design for a range of Mach numbers, multi-point optimizations are carried out to investigate the capabilities. The operating Mach number is assumed to be between 0.66 and 0.72. Seven Mach numbers, including 0.66, 0.67, 0.68, 0.69, 0.70, 0.71 and 0.72 are chosen as design points with equal weighting coefficients in Eq. (3). All of other settings are kept the same as that in the previous single-point optimizations.

The comparison of optimized results for bump and vortex generating bump is presented in Table 5 and Fig. 13. Note this is for the same optimized design at different Mach numbers, while Fig. 5 is for different designs at different Mach. It can be seen that the optimized vortex generating bump could significantly reduce the overall drag at high transonic Mach numbers in comparison with the baseline. In contrast, the performance of the optimized contour bump at high operating Mach numbers is much worse than that of the bump with fins. Therefore, a well-designed vortex generating bump could offer

a more robust design to improve the performances of aircrafts operating at high transonic Mach numbers as a passive control device. Fig. 13 also shows a slight degradation of the vortex generating bump as compared with the contour bump at the lower transonic range in this multi-point optimization. It can be explained by the vortices produced by the vortex generators as shown in Fig.14, which clearly shows two streamwise vortices after the bump at each operating Mach number. The exist of streamwise vortices results in extra viscous drag at low operating Mach number, but it greatly improve the overall performances of the vortex generating bump at a wide range of operating Mach numbers.

Table 5 Results of multi-point optimizations.

Bump type	Bump crest	Relative crest	Bump height	VG crest	VG height	VG z1	VG z2
Contour bump	0.6709c	64.7%	0.0222c	-	-	-	-
Vortex generating bump	0.6937c	69.2%	0.0215c	0.5552c	0.0085c	70.0%	49.5%

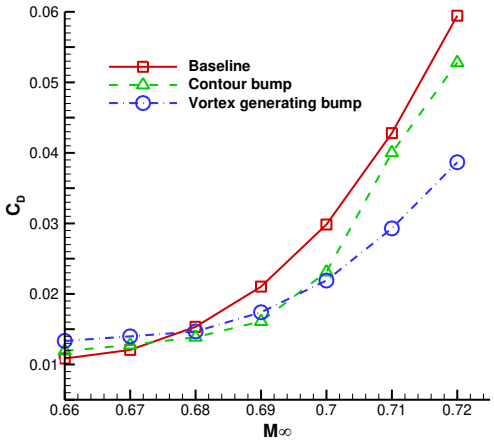

Fig. 13 Multi-point optimizations at C_L=0.82.

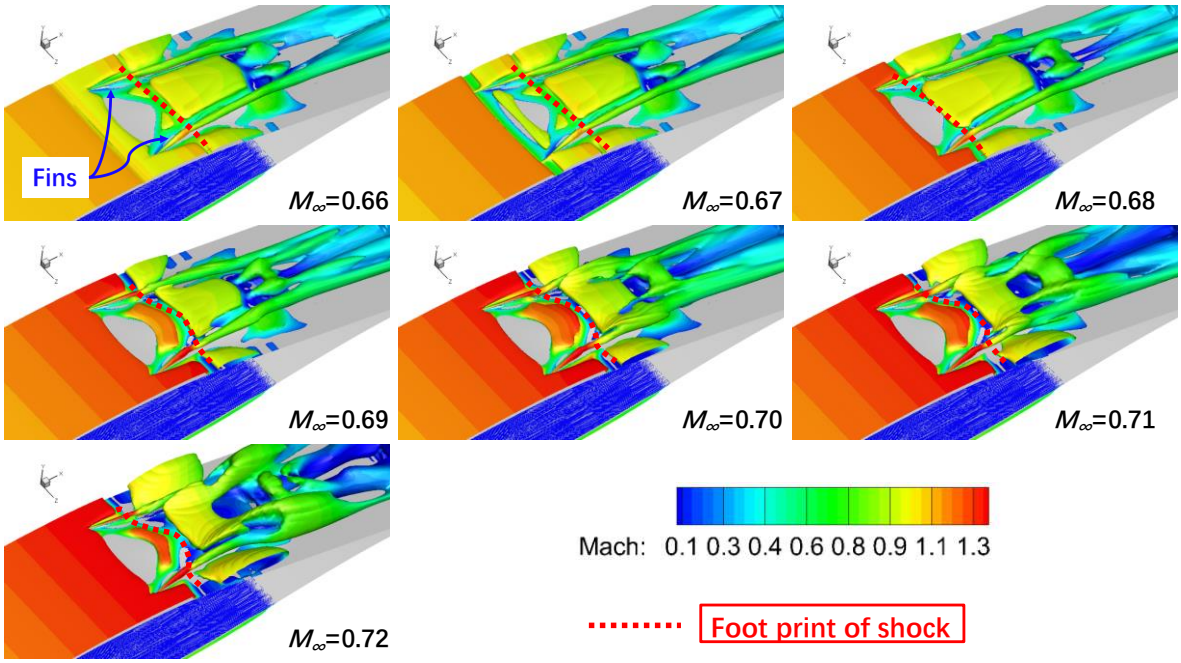

Fig. 14 Iso-surfaces of the optimized vortex generating bump at different operating Mach numbers (Q criterion = 1).

4 Conclusion

The integration of the 3D contour shock control bump with vane-type vortex generators has been proposed, parameterized, optimized and analyzed. In the optimization studies based on the Reynold-average Navier-Stokes equations, the trade-off between shock control and flow separation is revealed. It is found that a pair of vane-type vortex generating fins can be used to significantly improve the performances of the original contour shock control bumps at high transonic Mach numbers. The streamwise vortices triggered by the vortex generating fins can deliver substantial momentum into the region after the bump and significantly reduce the extent of flow separations. Overall, in comparison with shock control bumps, vortex generating bumps are proved to be useful in reducing drag and suppressing flow separations at higher transonic Mach numbers with a high C_L. The multi-point optimized combination of contour bump and vortex generators can offer a robust design for controlling shock wave and flow separations simultaneously at a range of transonic speeds with a high C_L. The vortex generating bumps can be designed as either active or passive flow control devices for a wide range of applications, such as buffet alleviation.

Acknowledgments

This research was initially sponsored by a University of Sheffield pump priming research fund, which also supported the first author's stay at the University of Sheffield to conduct the research. Further research on the project was funded by the projects supported by National Natural Science Foundation of China (No. 11672132, 12032011 and 11502112). The authors also acknowledge Lo and Kontis of the University of Glasgow for providing the experimental surface oil flow image in Fig. 12(a).

References

[1] Bushnell, D. M., "Shock Wave Drag Reduction." *Annual Review of Fluid Mechanics*, Vol. 36, 2004, pp. 81–96. https://doi.org/10.1146/annurev.fluid.36.050802.122110.

[2] Stanewsky, E., Délery, J., Fulker J., and Geißler, W., "Synopsis of the Project EUROSHOCK. Notes on Numerical Fluid Mechanics: EUROSHOCK - Drag Reduction by Passive Shock Control, Results of the Project EUROSHOCK." *Friedr. Vieweg & Sohn Verlagsgesellschaft mbH, Braunschweig/Wiesbaden*, Vol. 56, 1997, pp. 1–87.

[3] Stanewsky, E., Délery, J., Fulker, J., and De Matteis, P., "Synopsis of the Project EUROSHOCK II. Notes on Numerical Fluid Mechanics and Multidisciplinary Design: Drag Reduction by Shock and Boundary Layer Control-Results of the Project EUROSHOCK II." *Springer-Verlag Berlin Heidelberg*, Vol. 80, 2002, pp. 1–124.

[4] Tai, T. C., "Theoretical Aspects of Dromedaryfoil." *David W. Taylor Naval Ship Research and Development Center, Tech. Report no. 770104*, 1977.

[5] Tai, T. C., Huson, G. G., Hicks, R. M., and Gregorek, G. M., "Transonic Characteristics of a Humped Airfoil." *Journal of Aircraft*, Vol. 25, No. 8, 1988, pp. 673–674. https://doi.org/10.2514/3.45642.

[6] Ashill, P., Fulkner, J. and Shires, A. A., "A Novel Technique for Controlling Shock Strength of Laminar Flow Aerofoil Sections." *DGLR Bericht, Pt. 6,* 1992, pp. 175–183.

[7] Fulker, J. L., Ashill, P. R., and Simmons M. J., "Study of Simulated Active Control of Shock Waves on an Aerofoil." *Defence Research Agency, Technical. Rept. TR93025,Farnborough: Defence Research Agency*, 1993.

[8] Birkemeyer, J., Rosemann, H., and Stanewsky, E., "Shock Control on a Swept Wing." *Aerospace Science and Technology*, Vol. 4, No. 3, 2000, pp. 147–156. https://doi.org/10.1016/S1270-9638(00)00128-0.

[9] Qin, N., Monet, D., and Shaw, S. T., "3D Bumps for Transonic Wing Shock Control and Drag Reduction." *CEAS Aerospace Aerodynamics Research Conference, Cambridge, UK*, 2002.

[10] Qin, N., Wong, W. S., and Le Moigne, A., "Three-Dimensional Contour Bumps for Transonic Wing Drag Reduction." *Proceedings of the Institution of Mechanical Engineers, Part G: Journal of Aerospace Engineering*, Vol. 222, No. 5, 2008, pp. 619–629. https://doi.org/10.1243/09544100JAERO333.

[11] Wong, W. S., Le Molgne, A., and Qin, N., "Parallel Adjoint-Based Optimisation of a Blended Wing Body Aircraft with Shock Control Bumps." *Aeronautical Journal*, Vol. 111, No. 1117, 2007, pp. 165–174. https://doi.org/10.1017/S0001924000004425.

[12] Wong, W. S., Qin, N., Sellars, N., Holden, H., and Babinsky, H., "A Combined Experimental and Numerical Study of Flow Structures over Three-Dimensional Shock Control Bumps." *Aerospace Science and Technology*, Vol. 12, No. 6, 2008, pp. 436–447. https://doi.org/10.1016/j.ast.2007.10.011.

[13] Ogawa, H., Babinsky, H., Pätzold, M., and Lutz, T., "Shock-Wave/Boundary-Layer Interaction Control Using Three-Dimensional Bumps for Transonic Wings." *AIAA Journal*, Vol. 46, No. 6, 2008, pp. 1442–1452. https://doi.org/10.2514/1.32049.

[14] König, B., Pätzold, M., Lutz, T., Krämer, E., Rosemann, E., Richter, K., and Uhlemann, H., "Numerical and Experimental Validation of Three-Dimensional Shock Control Bumps." *Journal of Aircraft*, Vol. 46, No. 2, 2009, pp. 675–682. https://doi.org/10.2514/1.41441.

[15] Colliss, S. P., Babinsky, H., Nöbler, K., and Lutz, T., "Vortical Structures on Three-Dimensional Shock Control Bumps." *Journal of Aircraft*, Vol. 54, No. 8, 2016, pp. 2338–2350. https://doi.org/10.2514/1.J054669.

[16] Bruce, P. J. K., and Colliss, S. P., "Review of Research into Shock Control Bumps." *Shock Waves*, Vol. 25, 2015, pp. 451–471. https://doi.org/10.1007/s00193-014-0533-4.

[17] Deng, F., Qin, N., Liu, X., Yu, X., and Zhao, N., "Shock Control Bump Optimization for a Low Sweep Supercritical Wing." *Science China Technological Sciences*, Vol. 56, No. 10, 2013, pp. 2385–2390. https://doi.org/10.1007/s11431-013-5345-8.

[18] Jones, N. R., Eastwood, J. P., and Jarrett, J. P., "Adapting Three-Dimensional Shock Control Bumps for Swept Flows." *AIAA Journal*, Vol. 55, No. 3, 2017, pp. 861–873. https://doi.org/10.2514/1.J055169.

[19] Zhou, L., Chen, D. H., Tao, Y., Liu, G. Y., Song, S. H., and Zhong, S. D., "Passive Shock Wave/Boundary Layer Control of Wing at Transonic Speeds." *Theoretical and Applied Mechanics Letters*, Vol. 7, No. 6, 2017, pp. 325–330. https://doi.org/10.1016/j.taml.2017.11.006.

[20] Hinchliffe, B., and Qin, N., "Using Surface Sensitivity from Mesh Adjoint for Transonic Wing Drag Reduction." *AIAA Journal*, Vol. 55, No. 3, 2017, pp. 818–831. https://doi.org/10.2514/1.J055319.

[21] Jones, N. R., and Jarrett, J. P., "Designing a Shock Control Bump Array for a Transonic Wing-Body Model." *AIAA Journal*, Vol. 56, No. 12, 2018, pp. 4801–4814. https://doi.org/10.2514/1.J056725.

[22] Zhu, M., Li, Y., Qin, N., Huang, Y., Deng, F., Wang, Y., and Zhao, N., "Shock Control of a Low-Sweep Transonic Laminar Flow Wing." *AIAA Journal*, Vol. 57, No. 6, 2019, pp. 2408–2420. https://doi.org/10.2514/1.J058011.

[23] Deng, F., and Qin, N., "Quantitative Comparison of 2D and 3D Shock Control Bumps for Drag Reduction on Transonic Wings." *Proceedings of the Institution of Mechanical Engineers, Part G: Journal of Aerospace Engineering*, Vol. 233, No. 7, 2019, pp. 2344–2359. https://doi.org/10.1177/0954410018778815.

[24] Jinks, E., Bruce, P. J. K., and Santer, M., "Optimisation of Adaptive Shock Control Bumps with Structural Constraints." *Aerospace Science and Technology*, Vol. 77, 2018, pp. 332–343. https://doi.org/10.1016/j.ast.2018.03.018.

[25] Gramola, M., Bruce, P. J. K., and Santer, M., "Experimental FSI Study of Adaptive Shock Control Bumps." *Journal of Fluids and Structures*, Vol. 81, 2018, pp. 361–377. https://doi.org/10.1016/j.jfluidstructs.2018.05.005.

[26] Gramola, M., Bruce, P. J. K., and Santer, M., "Off-Design Performance of 2D Adaptive Shock Control Bumps." *Journal of Fluids and Structures*, Vol. 93, 2020, p. 102856. https://doi.org/10.1016/j.jfluidstructs.2019.102856.

[27] Eastwood, J. P., and Jarrett, J. P., "Toward Designing with Three-Dimensional Bumps for Lift/Drag Improvement and Buffet Alleviation." *AIAA Journal*, Vol. 50, No. 12, 2012, pp. 2882–2898. https://doi.org/10.2514/1.J051740.

[28] Tian, Y., Gao, S. Q., Liu, P. Q., and Wang, J. J., "Transonic Buffet Control Research with Two Types of Shock Control Bump Based on RAE2822 Airfoil." *Chinese Journal of Aeronautics*, Vol. 30, No. 5, 2017, pp. 1681–1696. https://doi.org/10.1016/j.cja.2017.07.011.

[29] Mayer, R., Lutz, T., and Krämer, E., "Numerical Study on the Ability of Shock Control Bumps for Buffet Control." *AIAA Journal*, Vol. 56, No. 5, 2018, pp. 1978–1987. https://doi.org/10.2514/1.J056737.

[30] Mayer, R., Lutz, T., Krämer, E., and Dandois, J., "Control of Transonic Buffet by Shock Control Bumps on Wing-Body Configuration." *Journal of Aircraft*, Vol. 56, No. 2, 2019, pp. 556–568. https://doi.org/10.2514/1.C034969.

[31] Lin, J. C., "Review of Research on Low-Profile Vortex Generators to Control Boundary-Layer Separation." *Progress in Aerospace Sciences*, Vol. 38, Nos. 4–5, 2002, pp. 389–420. https://doi.org/10.1016/S0376-0421(02)00010-6.

[32] Lu, F. K., Li, Q., and Liu, C. Q., "Microvortex Generators in High-Speed Flow." *Progress in Aerospace Sciences*, Vol. 53, 2012, pp. 30–45. https://doi.org/10.1016/j.paerosci.2012.03.003.

[33] Panaras, A. G., and Lu, F. K., "Micro-Vortex Generators for Shock Wave/Boundary Layer Interactions." *Progress in Aerospace Sciences*, Vol. 74, 2015, pp. 16–47. https://doi.org/10.1016/j.paerosci.2014.12.006.

[34] Jones, D. R., Schonlau, M., and Welch, W. J., "Efficient Global Optimization of Expensive Black-Box Functions." *Journal of Global Optimization*, Vol. 13, 1998, pp. 455–492. https://doi.org/10.1023/A:1008306431147.

[35] Jones, D. R., "A Taxonomy of Global Optimization Methods Based on Response Surfaces." *Journal of Global Optimization*, Vol. 21, 2001, pp. 345–383. https://doi.org/10.1023/A:1012771025575.

[36] Powell, M. J. D., "The BOBYQA Algorithm for Bound Constrained Optimization without Derivatives." *Centre for Mathematical Sciences. Rept. DAMTP 2009/NA06, University of Cambridge, UK*, 2009, pp. 26–46.

[37] Website. https://cfl3d.larc.nasa.gov/. Assessed on November 4, 2020.

[38] Sclafani, A. J., DeHaan, M. A., Vassberg, J. C., Rumsey, C. L., and Pulliam, T. H., "Drag Prediction for the Common Research Model Using CFL3D and OVERFLOW." *Journal of Aircraft*, Vol. 51, No. 4, 2014, pp. 1101–1117. https://doi.org/10.2514/1.C032571.

[39] Fulker, J. L., and Simmons, M. J., "An Experimental Study of Shock Control Methods." *DRA/AS/HWA/TR94007/1*, 1994.

[40] Menter, F. R., "Two-Equation Eddy-Viscosity Turbulence Models for Engineering Applications." *AIAA Journal*, Vol. 32, No. 8, 1994, pp. 1595–1605. https://doi.org/10.2514/3.12149.

[41] Spalart, P. R., and Allmaras, S. R., "A One-Equation Turbulence Model for Aerodynamic Flows." *Recherche Aerospatiale*, Vol. 1, 1994, pp. 5–21.

[42] Allan, B. G., Yao, C. S., and Lin, J. C., "Numerical Simulations of Vortex Generator Vanes and Jets on a Flat Plate." *1st Flow Control Conference 24-26 June 2002, St. Louis, Missouri, AIAA 2002-3160*. https://doi.org/10.2514/6.2002-3160.

[43] Lo, K. H., and Kontis, K., "Supersonic Flow over Rounded Contour Bumps with Vortex Generators or Passive Longitudinal Jets." *Experimental Thermal and Fluid Science*, Vol. 85, 2017, pp. 213–228. https://doi.org/10.1016/j.expthermflusci.2017.03.005.